Effects of chordwise flexibility on 2D flapping foils used as an energy extraction device

Guillaume Jeanmonod[a,b], Mathieu Olivier[b,*]

[a] *Ecole Polytechnique Fédérale de Lausanne, CH-1015 Lausanne, Switzerland*

[b]*Laboratoire de Mécanique des Fluides Numérique, Department of Mechanical Engineering,
Université Laval, Quebec City, Quebec, G1V 0A6, Canada*

Abstract

The effects of chordwise pressure- and inertia-driven deformations on the power extraction potential of a kinematically constrained oscillating thin plate that undergoes a heaving and pitching motion are investigated. 2D fully coupled fluid-structure interaction simulations are performed at a Reynolds number of 1100 with thin flexible plates having a thickness over chord ratio of 1%. Three flexibility distributions are tested: a uniformly flexible plate as well as plates with only the rear part or the front part being flexible. The results are compared with those of rigid plates operating at the same conditions. Flexible plates show very promising results as they can extract up to more than twice the power of the corresponding rigid ones. The investigation of semi-flexible foils has highlighted the fact that considering a completely flexible foil with constant chordwise mechanical properties is likely not an optimal configuration. Indeed, different mechanisms are beneficial whether the front part or the rear part of the foil is flexible: pressure-driven deformations usually increase the performances of front flexible foils while inertia-driven deformations are beneficial to rear flexible foils. In cases involving weak fluid-structure interactions (e.g.: heavy plate in a light fluid), the resonance of the first deformation mode of the plate's tail or head may appear. It is observed that this phenomenon can either deteriorate or improve the performances of the flapping plate. In this context, the dimensionless flexibility appears to be a key factor as it is involved in the resonance phenomenon that turns out to greatly influence the flow field.

Keywords: flexible flapping wings, fluid-structure interaction, energy extraction, hydrokinetic turbine

1. Introduction

Nowadays, there is a global trend towards renewable energy sources. Sea current and river flows represent a large amount of renewable energy that is not fully exploited yet. The most widely used hydrokinetic turbines are rotating machines. The blade design is usually quite complex as it involves twisting and non-uniform chord length along the span. Taking its inspiration from the animal world, the concept of an oscillating wing used as a power extraction device has been presented for the first time in 1981 by McKinney and DeLaurier (1981). Thereafter, this novel concept has been studied deeply by many researchers. These studies involve either prescribed motion (Kinsey and Dumas (2008, 2012, 2014); Ashraf et al. (2011)), semi-active motion (Shimizu et al. (2008); Zhu and Peng (2009)), and fully-passive motion (Peng and Zhu (2009); Young et al. (2013)) concepts. The main advantages of these flapping-foil energy harvesters are generally recognized as the simplicity of the shape (no twist or chord length variation is needed), the absence of centrifugal forces, a low tip speed (lower impact on aquatic fauna and navigation) and a rectangular swept area (Xiao and Zhu (2014)). The last point is particularly interesting in the case of shallow

---

*Corresponding author
Email addresses:* `guillaume.jeanmonod@epfl.ch` (Guillaume Jeanmonod), `mathieu.olivier@gmc.ulaval.ca` (Mathieu Olivier)

Nomenclature

c	chord length	$\hat{\mathbf{n}}$	unit surface normal vector
d	vertical extent of the foil motion	p	pressure field
C_M	moment coefficient	Re	Reynolds number
C_P	power coefficient	T	period
C_Y	vertical force coefficient	t	time
(d_x, d_y)	displacement vector field	U_∞	freestream velocity
E	Young modulus	$\mathbf{v}$	velocity vector field
e	foil thickness	x_P	pitching axis position (pivot point)
$\tilde{e}$	Green-Lagrange strain	α	angle of attack
$\mathbf{F}'$	force vector per unit span	α_{Eff}	effective angle of attack
f	frequency	$\tilde{\chi}$	curvature of the deformed beam
f^*	reduced frequency	δ_p^*	flexibility
h	heaving displacement	η	efficiency
h^*	normalized heaving amplitude	ν	kinematic viscosity
h_0	heaving amplitude	ρ	density
I'	beam cross-section area moment of inertia per unit span	Σ	pressure-to-inertia ratio
		τ	shear load
M'	internal bending moment in a beam per unit span, moment per unit span	θ	pitching angle
		θ_0	pitching amplitude
N'	internal normal force in a beam per unit span	θ_{Eff}	effective pitching angle

water where the turbines diameter is limited by the water depth. Furthermore, it has been shown by Kinsey et al. (2011) that the efficiency of this concept can be comparable with more conventional hydrokinetic energy harvesters such as horizontal-axis and vertical-axis turbines.

While the concept of oscillating foil hydrokinetic turbine has been (and still is) thoroughly investigated, very few research has been done on the effect of wing flexibility of such turbines and the latter remains to be fully understood (Xiao and Zhu (2014)). On the other hand, the effect of wing flexibility has been extensively studied in propulsion applications based on flapping wings. Various physical mechanisms and phenomena such as inertia and pressure based deformations (Daniel and Combes (2002); Zhu (2007); Olivier and Dumas (2016)), force re-orientation (Katz and Weihs (1978); Heathcote and Gursul (2007)), and resonance (Ramananarivo et al. (2011); Kang et al. (2011); Dewey et al. (2013); Quinn et al. (2014); Zhu et al. (2014); Xu et al. (2016)) have been assessed.

First attempts in describing the effects of chordwise flexibility in flapping wing hydrokinetic turbines were proposed by Liu et al. (2013), Hoke et al. (2015), Zhu et al. (2015), and Le and Ko (2015). In all these studies, the wing deformation or camber is prescribed and the effects on the flow and the energy extraction are investigated with numerical simulations. It has been found that wing deformation can be beneficial for energy extraction if it is tuned properly. According to Liu et al. (2013) and Hoke et al. (2015), the investigation of the effects of flexibility using a fully coupled fluid-structure algorithm is the logical next step. Such a study has been published recently by Wu et al. (2015a,b) who conducted a numerical investigation of the effect of passive chordwise flexibility. Their study takes into consideration the actual fluid-structure coupling that causes the deformation of a flexible flat plate attached to a NACA profile trailing edge. Their results suggest that chordwise flexibility can increase significantly the efficiency and the power extraction of both fully-constrained and semi-active flapping-foil turbine concepts by increasing the lift force on the foil. More recently, Liu et al. (2016) also proposed a similar study, this time by considering a wing with an actual flexible trailing edge made of either real or virtual materials. They recorded increases in efficiency up to 32.2% with wings having a flexible tail. Moreover, they observed better performances with relatively low rigidity and mass ratio.

This paper presents a systematic investigation on the effects of pressure- and inertia-driven deformations on the performances of a chordwise flexible flapping foil used as an energy extraction device. The study takes into account three different chordwise flexibility distributions i.e., completely flexible foils as well as foils with the flexibility limited to the front part and the rear part only. A fully coupled fluid-structure algorithm is used to perform numerous 2D laminar numerical simulations of flexible or partly flexible foils. The simulations are performed at a Reynolds number of 1100 and the effects of varying the oscillation frequency, the pitching amplitude, and the foil mechanical properties are explored. Section 2 presents the problem definition. Section 3 presents an overview of the numerical methods as well as the verification and validation of the numerical tools. Finally, Section 4 presents the results of the numerical simulations and discusses the potential benefits of using chordwise flexibility in hydrokinetic turbine blades.

2. Problem definition

The flapping foil used in this study is actually a flexible flat plate of thickness $e = 0.01c$ with rigid rounded edges that oscillates in an upstream flow U_∞. While most studies of flapping-wing turbines use NACA profiles, Kinsey and Dumas (2008) have shown that the profile shape does not have major effects at a low Reynolds number of 1100, which is used throughout this study. Moreover, using a thin flat plate emphasizes the effects of foil flexibility. The foil motion is imposed on the pivot point (P in Fig. 1) which is located at the one-third chord and it consists of a combined heaving and pitching harmonic motion given by:

$$h(t) = h_0 \cos(2\pi f t),$$
$$\theta(t) = \theta_0 \sin(2\pi f t),$$

where h_0 and θ_0 are respectively the heaving and pitching amplitudes and f is the motion frequency. The instantaneous angle of attack (Anderson et al. (1998)) and the corresponding effective angle of attack that takes into account the foil deformation are respectively given by:

$$\alpha(t) = \arctan\left(-\frac{\dot{h}(t)}{v_x}\right) - \theta(t).$$
$$\alpha_{\text{Eff}}(t) = \arctan\left(-\frac{\dot{h}(t)}{v_x}\right) - \theta_{\text{Eff}}(t),$$

where θ_{Eff} is the instantaneous effective pitching angle. The problem configuration is depicted in Fig. 1. Three foil configurations are considered in this study:
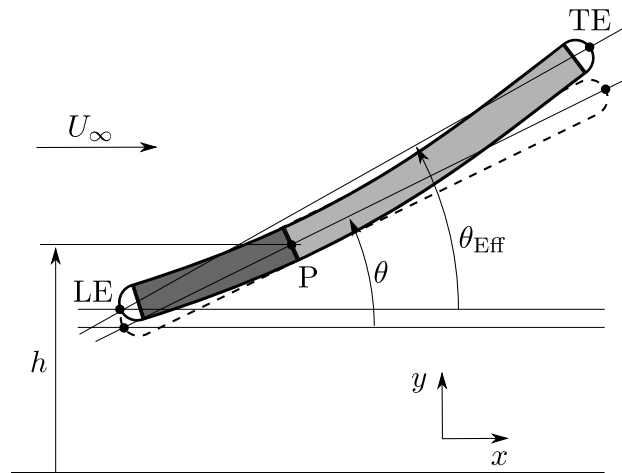

Figure 1: Motion description and wing geometry.

1. **Completely flexible foil:** the foil is completely flexible (light-gray and dark-gray regions in Fig. 1) except for the small rounded edges.

2. **Front flexible foil:** only the front part of the foil, also referred to as the head, is flexible (the dark-gray region in Fig. 1).

3. **Rear flexible foil:** only the rear part of the foil, also referred to as the tail, is flexible (the light-gray region in Fig. 1).

The idea of using front and rear flexibility is similar to the work of Liu et al. (2013), but here, the foil deformation is passive rather than being imposed. For a better understanding of the individual contributions of the head and the tail deformations to the effective angle of attack, $\Delta\alpha_{\text{head}}$ and $\Delta\alpha_{\text{tail}}$ are defined as follows:

$$\begin{aligned}
\Delta\alpha_{\text{head}}(t) &= \alpha_{\text{Eff, rt}}(t) - \alpha(t), \\
\Delta\alpha_{\text{tail}}(t) &= \alpha_{\text{Eff, rh}}(t) - \alpha(t),
\end{aligned} \tag{1}$$

where the subscripts rt and rh stand for *rigid tail* and *rigid head* respectively. $\alpha_{\text{Eff, rt}}$ is a fictive effective angle of attack computed with the actual position of the LE (solid line in Fig. 1) and the position of the TE as if the rear was rigid (dashed line in Fig. 1). $\alpha_{\text{Eff, rh}}$ is computed in the same way as $\alpha_{\text{Eff, rt}}$, but by considering the rigid position of the LE and the actual position of the TE.

The foil deformation is governed by a geometrically nonlinear Euler-Bernoulli beam model (see Epstein and Murray (1976)). The model takes into account axial and transverse displacements, respectively d_x and d_y, through the following coupled differential equations written in a total Lagrangian description:

$$\rho_s e \frac{\partial^2 d_x}{\partial t^2} = \frac{\partial}{\partial x}\left[N'\left(1 + \frac{\partial d_x}{\partial x}\right)\right] + \frac{\partial}{\partial x}\left[M'\frac{\partial^2 d_y}{\partial x^2}\right] + \frac{\partial^2}{\partial x^2}\left[M'\frac{\partial d_y}{\partial x}\right] - p\frac{\partial d_y}{\partial x} + \tau\left(1 + \frac{\partial d_x}{\partial x}\right),$$

$$\rho_s e \frac{\partial^2 d_y}{\partial t^2} = \frac{\partial}{\partial x}\left[N'\frac{\partial d_y}{\partial x}\right] - \frac{\partial^2}{\partial x^2}\left[M'\left(1 + \frac{\partial d_x}{\partial x}\right)\right] - \frac{\partial}{\partial x}\left[M'\frac{\partial^2 d_x}{\partial x^2}\right] - p\left(1 + \frac{\partial d_x}{\partial x}\right) - \tau\frac{\partial d_y}{\partial x},$$

where p and τ are respectively the fluid pressure and the fluid shear stress acting on the deformed configuration of the foil while ρ_s is the foil density. Note that, in the following, subscripts s and f are used to identify respectively solid and fluid quantities. These equations are then closed by using the Euler-Bernoulli beam theory to express the normal force N' and the internal bending moment M' as follows:

$$N' = Ee\tilde{e} = Ee\left[\frac{\partial d_x}{\partial x} + \frac{1}{2}\left(\left(\frac{\partial d_x}{\partial x}\right)^2 + \left(\frac{\partial d_y}{\partial x}\right)^2\right)\right],$$

$$M' = EI'\tilde{\chi} = EI'\left[\frac{\partial^2 d_y}{\partial x^2}\left(1 + \frac{\partial d_x}{\partial x}\right) - \frac{\partial d_y}{\partial x}\frac{\partial^2 d_x}{\partial x^2}\right],$$

where $\tilde{e}$ is the Green-Lagrange strain and $\tilde{\chi}$ is the modified curvature of the deformed beam as defined by Epstein and Murray (1976). On the other hand, the flow field is represented by the incompressible Navier-Stokes equations:

$$\frac{\partial \mathbf{v}}{\partial t} + \mathbf{v} \cdot \nabla\mathbf{v} = -\nabla\left(\frac{p}{\rho_f}\right) + \nu\nabla^2\mathbf{v},$$

$$\nabla \cdot \mathbf{v} = 0,$$

where $\mathbf{v}$ and p are respectively the velocity and pressure fields while ρ_f and ν are respectively the density and the kinematic viscosity of the fluid. Momentum and mass conservation yields the following conditions at the fluid-solid interface:

$$\begin{aligned}
\mathbf{v}_f &= \mathbf{v}_s, \\
\hat{\mathbf{n}} \cdot \boldsymbol{\sigma}_f &= \hat{\mathbf{n}} \cdot \boldsymbol{\sigma}_s,
\end{aligned}$$

where $\boldsymbol{\sigma}$ is the Cauchy stress field.

2.1. Parametric space

The dimensionless parameters of this problem are chosen to be the same as those presented by Olivier and Dumas (2016). This parameter set is consistent with that typically used in flapping foil energy harvester studies (Kinsey and Dumas (2008)), but it also contains two more parameters that are related to the structural dynamics of the foil and its interaction with the flow. The first structural parameter is the pressure-to-inertia ratio Σ, which represents the ratio of pressure forces acting on the foil over inertia forces caused by the foil mass. The second structural parameter is the flexibility δ_p^*, which provides an estimation of the foil deflection resulting from pressure forces acting on it. Strong fluid-solid interactions occur when both Σ and δ_p^* are high. In such a scenario, the structure deformation is caused by the pressure coming from the flow, which is itself significantly influenced by the large deformation of the structure that it causes. The complete parameter set is presented in Table 1.

Table 1: Dimensionless parameters for the flexible flapping-foil problem.

Name	Definition
Reynolds number	$Re = \dfrac{U_\infty c}{\nu}$
Reduced frequency	$f^* = \dfrac{fc}{U_\infty}$
Normalized heaving amplitude	$h^* = \dfrac{h_0}{c}$
Pitching amplitude	θ_0
Pressure-to-inertia ratio	$\Sigma = \dfrac{\rho_f h_0}{\rho_s e}$
Flexibility	$\delta_p^* = \dfrac{\rho_f (h_0 f)^2 c^3}{EI'}$

2.2. Performance metrics

The performances of a flapping foil in power extraction regime are evaluated using the power coefficient C_P and the efficiency η, which are respectively defined as:

$$
\begin{aligned}
C_P &= \frac{\mathbf{F}'_{\mathrm{P}} \cdot \hat{\mathbf{y}} \, \dot{h}}{\frac{1}{2}\rho_f U_\infty^3 c} + \frac{M'_{\mathrm{P}} \dot{\theta}}{\frac{1}{2}\rho_f U_\infty^3 c} \\
&= \underbrace{\frac{C_Y \, \dot{h}}{U_\infty}}_{C_{P,y}} + \underbrace{\frac{C_M \, \dot{\theta} \, c}{U_\infty}}_{C_{P,\theta}},
\end{aligned}
\tag{2}
$$

$$
\eta = \overline{C_P} \frac{c}{d},
$$

where the $\overline{()}$ represents the cycle-average while C_Y and C_M are respectively the vertical force and the moment coefficients acting on the pivot point. These definitions are very similar to those proposed in the literature (Kinsey and Dumas (2008, 2014); Peng and Zhu (2009); Ashraf et al. (2011)), among others), but they differ in two aspects:

1. The force $\mathbf{F}'_{\mathrm{P}}$ and the moment M'_{P} (as well as their respective coefficients) are the structural reactions per unit span (denoted by the prime symbol) occurring at the pivot point rather than the aerodynamic reactions on the foil surface.
2. The vertical extent of the foil motion d takes into account the foil deformation.

The actual aerodynamic force coefficients can also be computed by using the aerodynamic force and moment, $\mathbf{F}'_{\text{aero}}$ and M'_{aero}, acting on the foil instead of $\mathbf{F}'_{\text{P}}$ and M'_{P}. For example, $C_{Y,\text{aero}}$ yields:

$$C_{Y,\text{aero}} = -\frac{\mathbf{F}'_{\text{aero}} \cdot \hat{\mathbf{y}}}{\frac{1}{2}\rho_f U_\infty^2 cb}.$$

The instantaneous aerodynamic forces differ from the structural ones (those computed at point P) by an amount that represents the instantaneous inertial forces in the foil:

$$\mathbf{F}_{\text{P}} = \underbrace{-\int_{V_{\text{wing}}} \rho_s \dot{\mathbf{v}}\, dV}_{\text{Solid body inertia}} + \mathbf{F}_{\text{aero}}, \tag{3}$$

However, when the motion and the deformation of the foil are periodic, the aerodynamic cycle-averaged forces are the same as their corresponding structural ones (see Olivier and Dumas (2016) for further details).

In the present study, the cycle averaged coefficients are evaluated at each oscillation cycle. Once the difference between two successive cycles is below 1%, the simulation is considered to have reached its periodic state. However, large pitching amplitudes and very flexible foils may result in complex wake dynamics that may not reach a periodic state. In such cases, the averaging is made on more than one cycle in order to retain the effective performance.

3. Numerical methods, verification, and validation

The proposed flapping-foil problem is solved numerically with a dedicated partitioned fluid-structure interaction solver. The fluid flow is solved with a second-order finite-volume code based on the *OpenFOAM* library (OpenFOAM Foundation (2013)) while the beam equations are solved with an in-house finite-element code that uses Hermite shape functions. The fluid-solid interface conditions as well as the mesh motion in the fluid domain are handled by multivariate interpolation (radial basis functions). The numerical code has been extensively validated with various numerical experiments as well as with the experimental data of Heathcote and Gursul (2005, 2007). Further details on the code and on the validation can be found in Olivier (2014) and Olivier and Dumas (2016).

Regarding the verification of the numerical resolution for the present study, a typical simulation has been run on a coarse, medium, and fine mesh. For consistency, the time-step size and the residual tolerances are reduced with increasing mesh resolution. The numerical parameters of the simulations are summarized in Table 2. Each simulation is run over two cycles and the parameters used are:

$$Re = 1100, \quad h^* = 1, \quad \theta_0 = 60°, \quad f^* = 0.14, \quad \Sigma = 1, \quad \delta_p^* = 0.1447.$$

Table 2: Discretization characteristics and residual tolerances used for the verification of the numerical method.

	Coarse	Medium	Fine
Number of cells (fluid)	15,376	60,454	235,998
Number of beam elements (solid)	24	48	96
Time-step $\Delta t/T$	5×10^{-4}	2.5×10^{-4}	1.25×10^{-4}
Residual tolerance, pressure	$1e^{-6}$	$1e^{-7}$	$1e^{-8}$
Residual tolerance, velocity	$1e^{-6}$	$1e^{-7}$	$1e^{-8}$
Residual tolerance, displacement	$1e^{-5}$	$1e^{-6}$	$1e^{-7}$

Results from the first cycle (Table 3) shows a difference in $\overline{C_P}$ of 1.1% between the coarse and medium meshes and of 0.1% between the medium and fine meshes. The second cycle shows very similar results with a difference of 1.7% between the coarse and medium meshes and -0.16% between the medium and fine meshes.

6

Table 3: Mean power coefficient for the first and second cycle with the three meshes.

	Coarse	Medium	Fine
$\overline{C_P}$ (1st cycle)	0.6482	0.6414	0.6413
$\overline{C_P}$ (2nd cycle)	0.6005	0.5903	0.5913

Fig. 2 shows that the coarse mesh is much more dissipative than the medium and the fine meshes. However, the medium and fine meshes show very comparable vorticity fields near the foil. The aerodynamic forces (Fig. 3) of the fine and medium meshes are almost perfectly superimposed while there is a visible mismatch with the coarse mesh. With a relative difference on $\overline{C_P}$ below 0.2% and a lower computational cost compared to the fine mesh, the

(a)   (b)   (c)
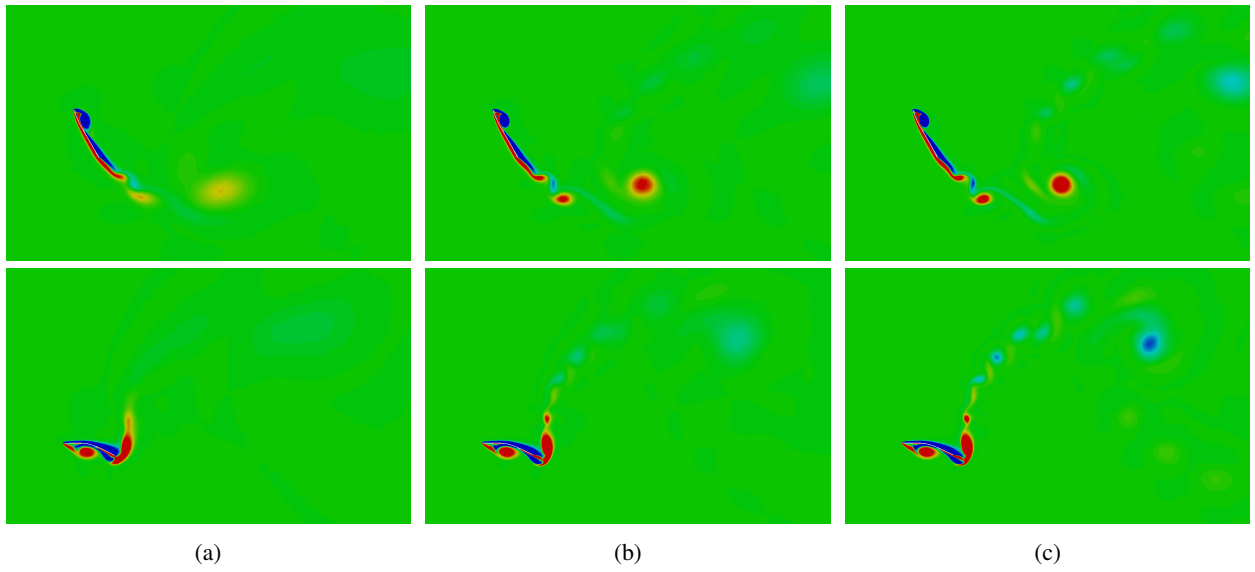
Figure 2: Vorticity field during the second cycle at t/T=0.5 (bottom) and 0.75 (top) for the three different meshes: (a) coarse mesh, (b) medium mesh, and (c) fine mesh.

(a)   (b)
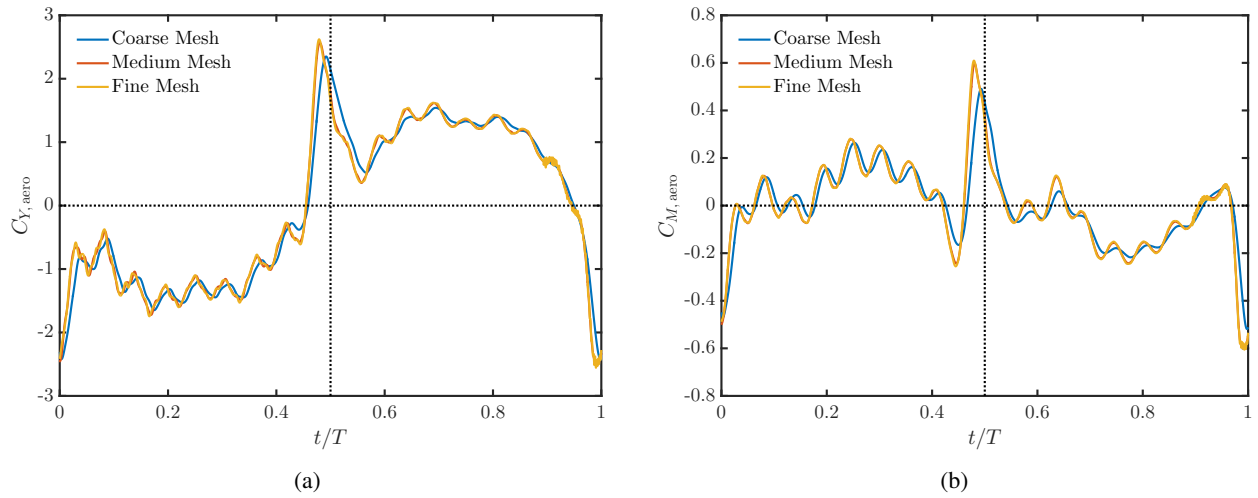
Figure 3: Vertical aerodynamic force (a) and moment (b) coefficients for the three level of mesh refinement

medium mesh appears to be a good trade-off between precision and computational effort for this work. Therefore, the latter was used to perform the parametric investigation. The time-step is chosen so that $\Delta t = T/4000$. Moreover, the time-step may be reduced further if needed to ensure that the maximum local Courant number remains small (on the order of 1).

4. Results and discussion

The effects of foil flexibility on the power coefficient of an oscillating-wing hydrokinetic turbine are explored for different flexibility distributions. Because the foil deformation generally changes the vertical extend d of the foil motion, considering either η or $\overline{C_P}$ as a performance metric may lead to opposite conclusions when it comes to select the optimal foil flexibility. Depending on the context, the more appealing metric may be either the efficiency or the extracted power coefficient. In this paper, the discussion focuses on the power coefficient following this reasoning: in a power plant that uses a rigid oscillating foil as a power extraction device, one may be interested in the power output increase produced by simply replacing the foil with a flexible one without any other modification. Nevertheless it is agreed that optimizing the efficiency may be desirable in other contexts. Therefore, a short discussion on efficiency is provided in Section 4.1.3.

In the upcoming discussion, results obtained for a completely flexible foil are presented and compared with a rigid foil. Afterwards, the flexibility of the foil is limited to the front part and to the rear part of the foil. These configurations are respectively referred to as *front flexible* and *rear flexible* and the separate effects of rear and front flexibility are presented. Similarly to Kinsey and Dumas (2008), all simulations were run with $Re = 1100$ and with $h^* = 1$. The related deformation mechanisms, namely pressure-based and inertia-based deformations, are also explored against the dimensionless flexibility (δ_p^*).

It is worth pointing out that, in a real design, it is not trivial to control both the rigidity and the density of the foil simply by choosing a specific solid materials since those properties cannot be changed for a given material. However, Σ and δ_p^* can be tuned by varying the thickness of the foil while having only minor effects on the aerodynamics as long as the relative thickness remains rather low (say no more than about 2 %, see Olivier (2014)). Moreover, using a composite foil structure or a nonuniform foil cross-section (which would change the relation between e and I') would allow a better control of the 2 dimensionless parameters with a given material. For example, in water applications, moderate pressure-driven deformations can be obtained by using a rubber foil with a steel stiffener. However, inertia-driven deformations would likely require a thicker foil made of heavy small components elastically linked with relatively soft materials. Indeed, while using a heavy thick wing allows the value of Σ to be reduced, it also increases significantly the stiffness. Nevertheless, the scope of this paper being to provide an understanding of the fundamental fluid-solid coupling mechanisms that may occur in a flapping-foil energy harvester, this study will not address the actual foil composition further.

4.1. Completely flexible foils

The mean power coefficients obtained with completely flexible foils are presented in Fig. 4. The results have been obtained with different motion configurations (θ_0 and f^*). These configurations have been chosen based on the results of Kinsey and Dumas (2008), the configuration of Fig. 4a corresponding to the best efficiency case obtained with a NACA 0015 profile. Results show that a completely flexible foil may greatly increase the power extraction potential compared to a rigid foil for some configurations. For example, a flexible foil characterized by $\Sigma = 1$ and $\delta_p^* = 0.211$ operating at $f^* = 0.18$ and $\theta_0 = 60°$ has a mean power coefficient that rises to 0.5623 which corresponds to more than twice that of the corresponding rigid foil which is 0.2792 (see Fig. 4c). Furthermore, Fig. 4b also shows significant improvements of $\overline{C_P}$ with $\Sigma = 1$ and $\Sigma = 10$ and the trend suggests that increasing flexibility further may result in even better improvements. Unfortunately, increasing the flexibility further in order to find the maximum produces very large deformations with strong foil curvature that cannot be handled properly by the mesh motion algorithm. In Fig. 4d, a maximum 15.9% increase of C_P with respect to the rigid case is found when $\Sigma = 0.1$ and $\delta_p^* = 0.03$. On the other hand, when a near-optimal configuration is used (Fig. 4a), it appears that the improvement potential of flexibility remains small. Thus, depending on the operating configuration, the effect of the flexibility on the power extraction is very different and the maximum mean power coefficient is reached at different δ_p^* and Σ. Generally, pressure-driven deformations appear to benefit cases with high pitching amplitude while inertia-driven deformations
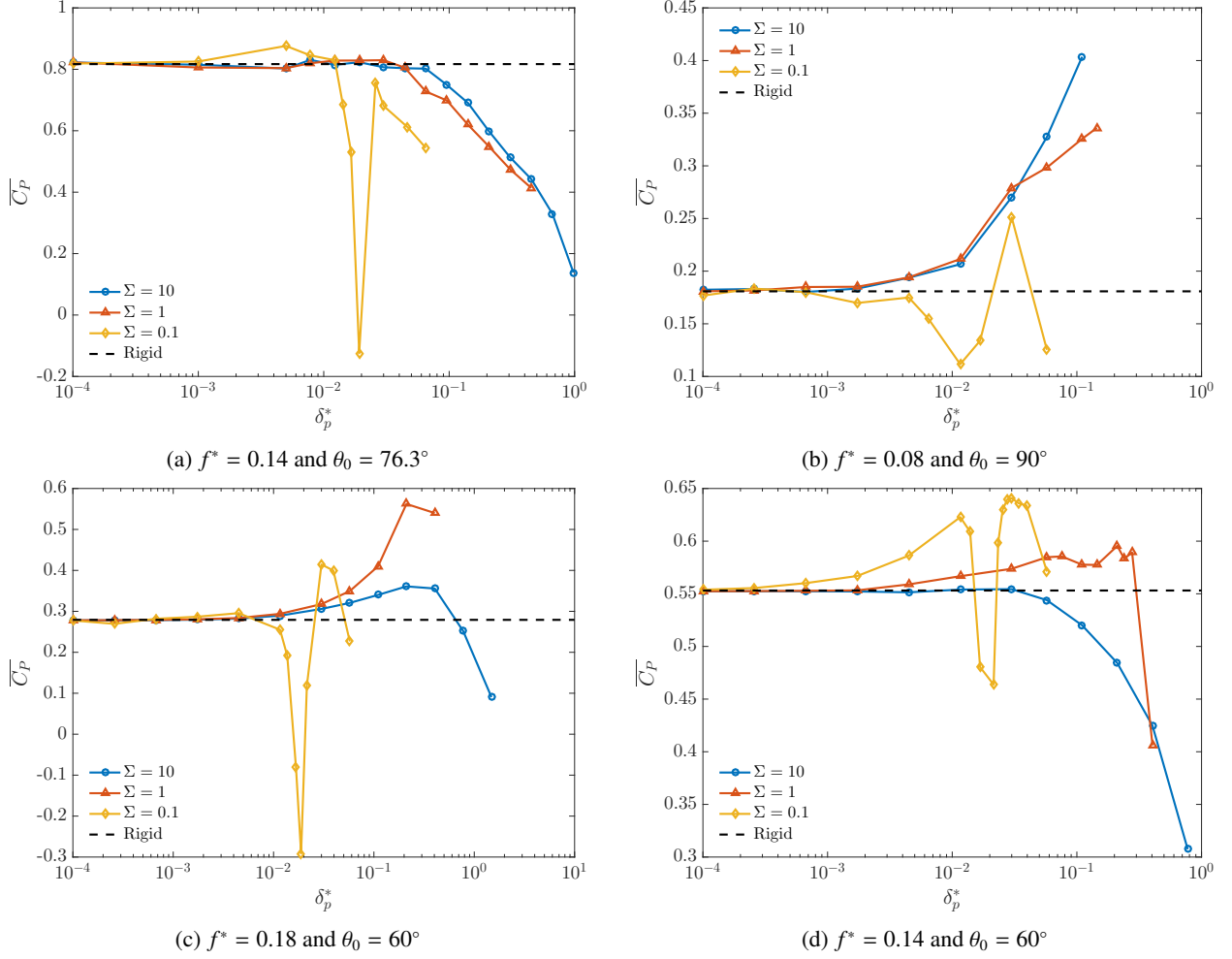
(a) $f^* = 0.14$ and $\theta_0 = 76.3°$

(b) $f^* = 0.08$ and $\theta_0 = 90°$

(c) $f^* = 0.18$ and $\theta_0 = 60°$

(d) $f^* = 0.14$ and $\theta_0 = 60°$

Figure 4: Mean power coefficient for different δ_p^* and Σ for a completely flexible foil.

give better performances for low pitching amplitude. The specific mechanisms explaining this general behavior are reported below in sections 4.1.1 and 4.1.2.

4.1.1. Effects of inertia-driven deformations

Inertia-driven deformations are dominant when Σ is low, that is, when the weight of the foil is relatively large when compared to pressure forces. The most striking feature of inertia-driven deformation cases ($\Sigma = 0.1$) is a large drop of the mean power coefficient that is observable in all cases reported in Fig. 4. This sudden drop, which occurs in a narrow range of δ_p^*, is caused by the excitation of the first bending mode of the tail when its corresponding natural frequency (f_1) is close to three times the oscillation frequency of the imposed motion f. The reason why the first deformation mode is triggered at a lower driving frequency is because of the coupled pitching and heaving motion. Indeed, the heaving acceleration transverse to the foil, which is responsible for the transverse inertial force that causes its bending, is $\ddot{h}(t)\cos(\theta(t))$ while the transverse acceleration caused by the rotation scales with $\ddot{\theta}(t)$. Adding these two contributions results in an inertial force that is a nonlinear superposition of harmonic function and whose periodic behavior can be decomposed as a sum of harmonic modes. The following quantity, γ, represents the normalized local transverse inertial force at a distance r from the pivot point:

$$\gamma = \cos(2\pi f t)\cos(\theta_0 \sin(2\pi f t)) + \left(\frac{r}{c}\right)\left(\frac{\theta_0}{h^*}\right)\sin(2\pi f t).$$

9

This force's evolution in time and its Fourier decomposition are shown in Fig. 5. Because the first half of the foil motion is antisymmetric with the second half, even modes do not exist. In these specific cases, the resonance is caused by the third harmonic and it results in a surprising behavior where the tail of the foil beats at a frequency that is three times faster than the motion frequency. This fast vibration results, in turn, in the power extraction degradation reported in Fig. 4 for cases with $\Sigma = 0.1$.
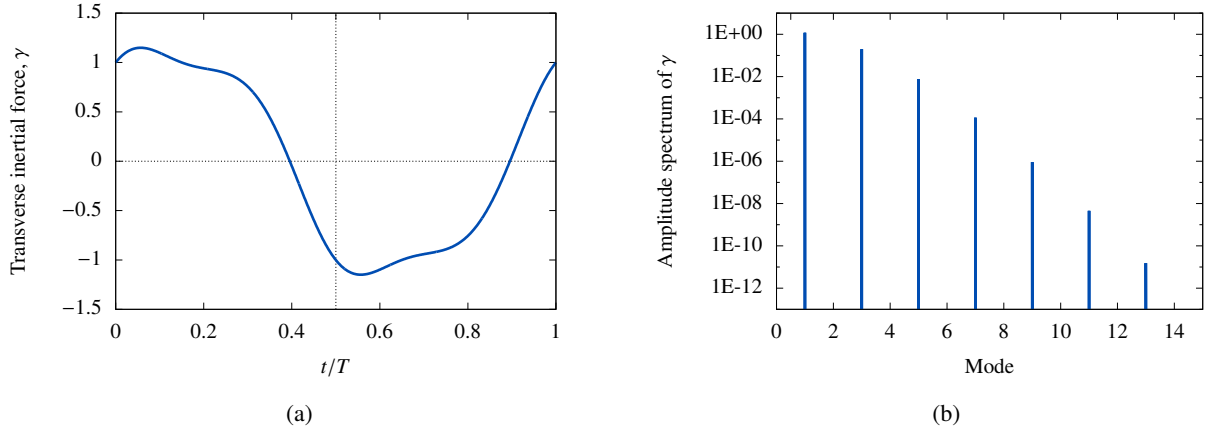
Figure 5: Representation of the normalized transverse inertial force γ: (a) instantaneous force obtained at the trailing edge of an underformed foil ($r/c = 2/3$) with $\theta_0 = 76.3°$ and $h^* = 1$, and (b) the corresponding Fourier decomposition.

The resonance observed in this study differs from that reported in previous flexible flapping foil studies (Dewey et al. (2013); Quinn et al. (2014); Xu et al. (2016); Liu et al. (2016)) since it is triggered by the driving motion harmonics rather than by the driving frequency itself. This particularity can readily be explained by the relatively high heaving amplitude used in the cases presented. Indeed, following the analysis of Young and Felgar (1949), a frequency ratio can be defined as:

$$\frac{f}{f_1} \simeq 1.787 \sqrt{\left(\frac{\delta_p^*}{\Sigma h^*} \right)}.$$

From this equation, it appears that, for resonance to be triggered by the driving frequency directly (not by its harmonics), the frequency ratio would need to be increased. For a given flexibility, this can be effectively done by decreasing the heaving amplitude h^*, but also by decreasing Σ. This is consistent with the findings of Xu et al. (2016) and Liu et al. (2016) since they have observed resonance by decreasing the mass ratio (which is essentially the inverse of Σ). Xu et al. (2016) and Quinn et al. (2014) have also reported the occurrence of higher vibration modes by using higher mass ratios and lower heaving amplitudes.

The effects of the foil deformation on the effective angle of attack and on the aerodynamic force coefficients are reported in Fig. 6 for the inertia-driven cases with $f^* = 0.18$ and $\theta_0 = 60°$. It is observed that the maximum and minimum α_{Eff} are shifted to the right as δ_p^* increases and a secondary peak is formed near the $t/T = 0$ and $t/T = 0.5$ (Fig. 6a at $\delta_p^* = 0.0116$). Then, when the natural frequency of the tail, which depends on δ_p^*, is close to three times the motion frequency, the foil undergoes the resonance phenomenon described earlier and α_{Eff} is composed of four well identifiable peaks (Fig. 6a at $\delta_p^* = 0.0167$). Even if this resonance phenomenon leads to high aerodynamic forces (Fig. 6b), it deteriorates the overall performances because both vertical and moment component of the aerodynamic forces are not in phase with their respective velocities. When the frequency is increased beyond the resonance (Fig. 6a at $\delta_p^* = 0.03$), α_{Eff} takes a more sinusoidal-like shape with a maximum shifted to the left compared to that of the rigid foil and the mean power coefficient returns to higher values.

A typical inertia-driven deformation case with a relatively low pitching amplitude of $\theta_0 = 60°$ (when compared to the nearly-optimal configuration with $\theta_0 = 76.3°$ reported by Kinsey and Dumas (2008)) is presented in Fig. 7. Fig. 7b shows that the inertial deformation of this flexible foil near the bottom end of the course ($t/T = 0.6$) generates a large pressure difference between the upper and the lower surface that pulls the foil in the heaving direction, when the
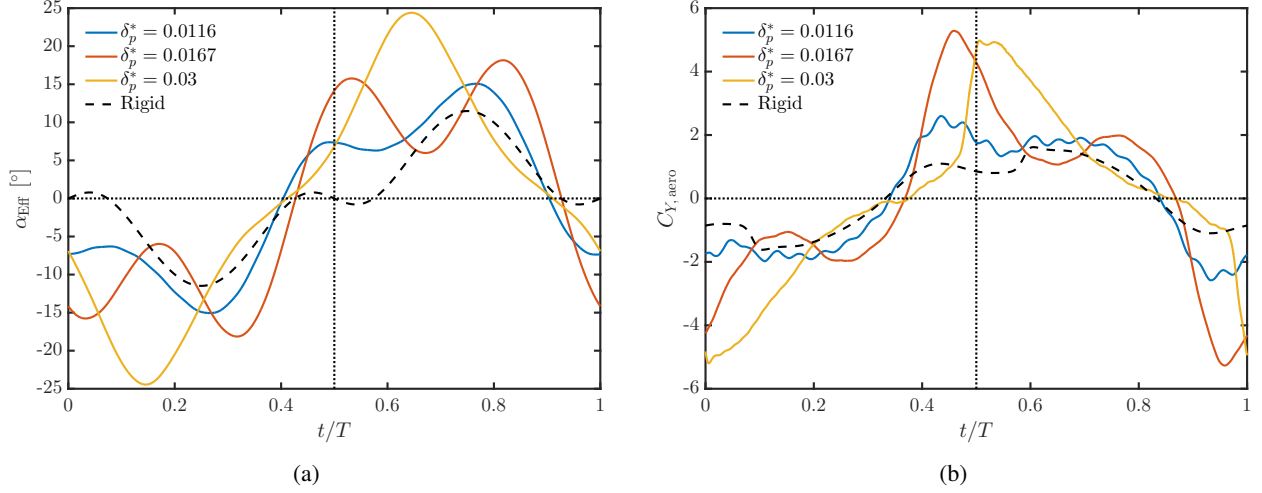
10

Figure 6: Comparison of (a) the effective angle of attack with the (b) vertical aerodynamic force coefficient with $f^* = 0.18$ and $\theta_0 = 60°$.

effective angle of attack is high. This pressure difference is much larger than that of a rigid foil observed at the same time (Fig. 7a). As a consequence, $C_{Y,\mathrm{aero}}$ and $C_{X,\mathrm{aero}}$ are greater (Fig. 8a). Nevertheless, C_P is negative at that time because the inertia resists to the vertical acceleration (Fig. 8b). The flexible foil also generates a larger Leading-Edge Vortex (LEV) (Fig. 7b at $t/T = 0.75$). When this LEV reaches the trailing edge, that is at $t/T = 0.9$, it covers a wider area and has a larger amplitude than that of a rigid foil (Fig. 7). This behavior is also reported by Le and Ko (2015) since their imposed deformation is similar to the passive deformation obtained with low Σ values. Moreover, at this same instant, the foil slows down and the inertia also participates positively to the power extraction.

While $C_{P,y}$ is relatively similar for both flexible and rigid foils, $C_{P,\theta}$ is almost always positive for the flexible foil and has a lower variation of amplitude (Fig. 8b). As a consequence, the amplitude of variation of C_P is larger for the flexible foil. It is worth noting that $C_{P,y}$ is negative on large time intervals in which the aerodynamic force appears to produce positive work output. The reason behind this counter-intuitive behavior is that $C_{P,y}$ takes into account not only the aerodynamic forces but also inertia forces, which are dominant when Σ is low (see Eqs. (2) and (3)).

On a more general perspective, the inertia of the foil when Σ is low has profound impacts on its power extraction performance, which can be either positive or negative. The general deformation pattern of such configurations is that the tail of the foil is thrown upward and downward respectively at the top and bottom ends of its course (the same pattern occurs with the head, but the effect is less important here because the head is shorter). Moreover, the rotational inertia helps in preserving this deformation during the downward and upward courses. This results in an increased effective pitching angle which may be beneficial if the nominal pitching amplitude θ_0 is lower than the optimal value. However, this deformation pattern is governed mostly by the time scale in the foil structure and its exact timing is not always well synchronized with the imposed motion. This becomes obvious when resonance is triggered by higher harmonics of the driving motion. In these situations, massive flow separations are likely to occur, and the output power generally decreases, although it is not excluded that beneficial resonance effects occur in other configurations. Low Σ configurations are also characterized by instantaneous reaction forces on the driving mechanism that differ largely in phase and in magnitude with the aerodynamic forces on the foil, the former having a higher amplitude.
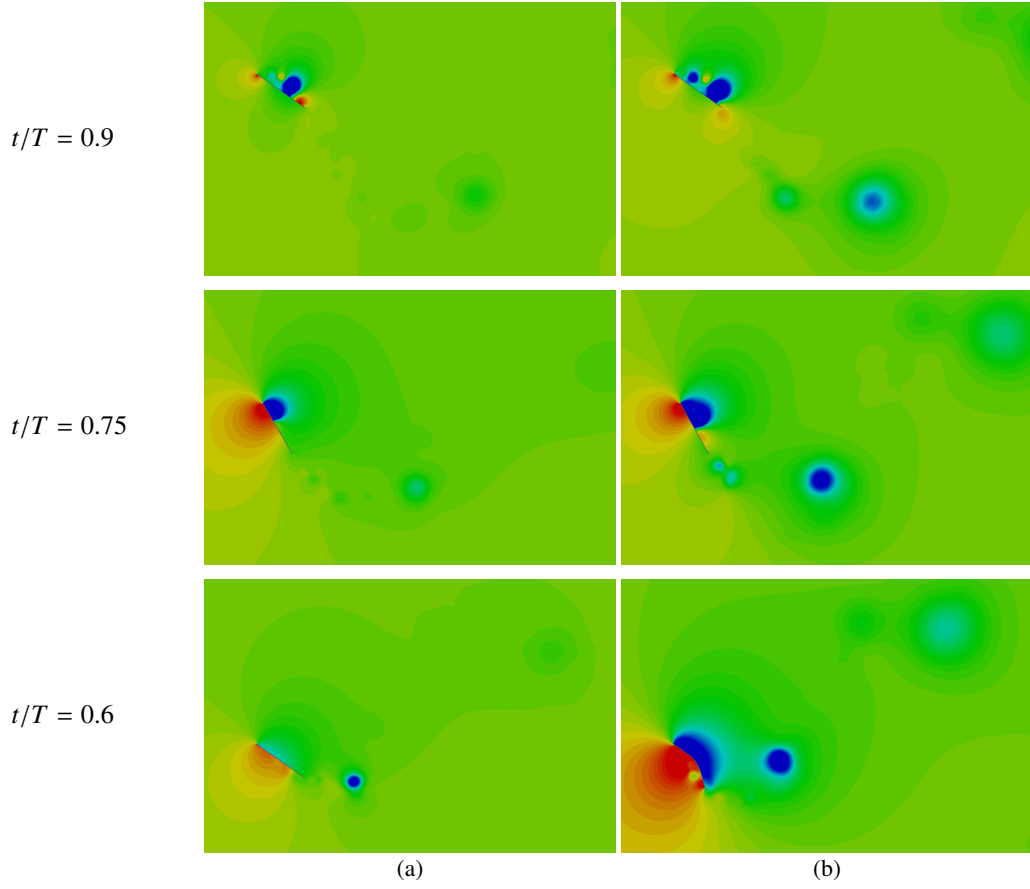
11

Figure 7: Instantaneous pressure fields with $f^* = 0.14$ and $\theta_0 = 60°$ around (a) a rigid foil and (b) a flexible foil ($\delta_p^* = 0.03$ and $\Sigma = 0.1$).
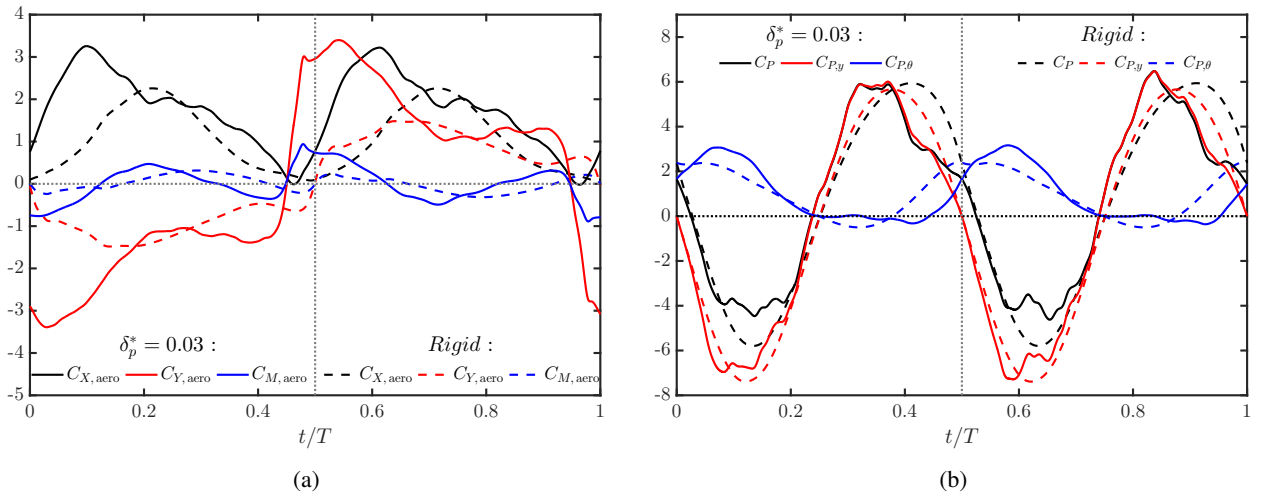

Figure 8: Comparison of a flexible and rigid foil with $\Sigma = 0.1$, $f^* = 0.14$, and $\theta_0 = 60°$: (a) the aerodynamic force coefficients and (b) the power coefficients.

4.1.2. Effects of pressure-driven deformations

When the pitching amplitude is large, pressure induced deformations on a completely flexible foil tend to reduce the effective angle of attack as δ_p^* increases (Fig. 9a) as opposed to inertia-driven deformations which firstly increase α_{Eff} and reduce it only in the second and fourth quarter of the cycle (Fig. 9b). This can be observed on Fig. 10 where the deflection of the trailing edge is not on the same side depending on the value of Σ. The pressure field variations observed in Fig. 10a are more intense than that in Fig. 10b. When $\Sigma = 0.1$ (Fig. 10a), the deformation is caused by the foil inertia and the foil motion increases the pressure difference between the lower side and the upper side of the foil. On the other hand, when $\Sigma = 10$ (Fig. 10b), it is actually the pressure difference that causes the deformation which results in a feathering effect similar to the one reported by Zhu (2007) and Olivier and Dumas (2016). Therefore the foil deformation mechanisms greatly differ with different Σ values. Note that different flexibilities have been used in the above comparison so that the actual foil deformation amplitude is similar in both cases. Indeed, in pressure-driven deformation cases, the foil deformation scales with δ_p^* while it scales with δ_p^*/Σ in inertia-driven deformation cases.
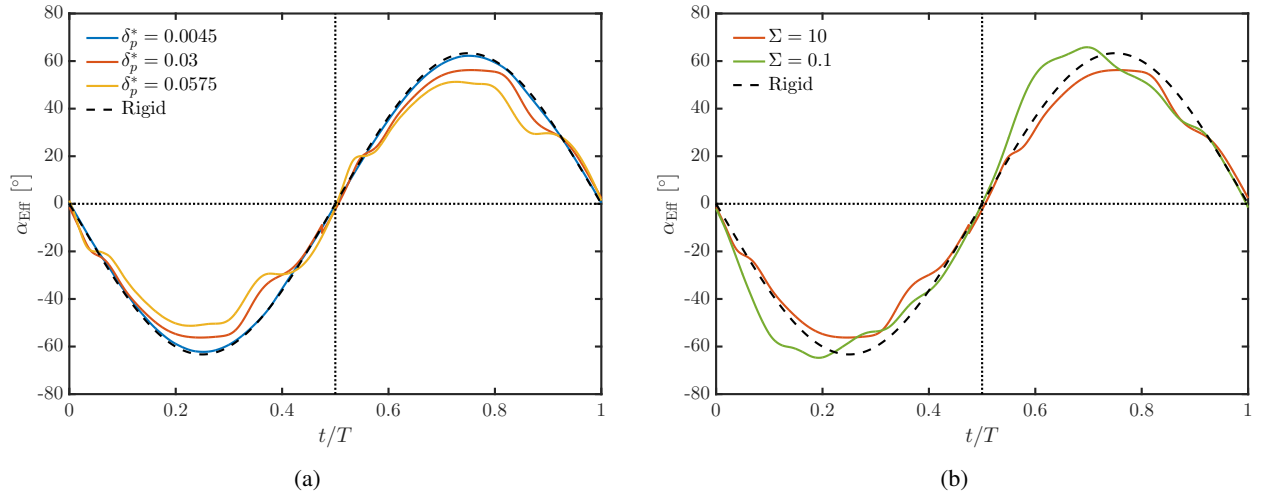
Figure 9: Effective angle of attack with $f^* = 0.08$ and $\theta_0 = 90°$: (a) $\Sigma = 10$ with different flexibilities, (b) $\delta_p^* = 0.03$ with different Σ.
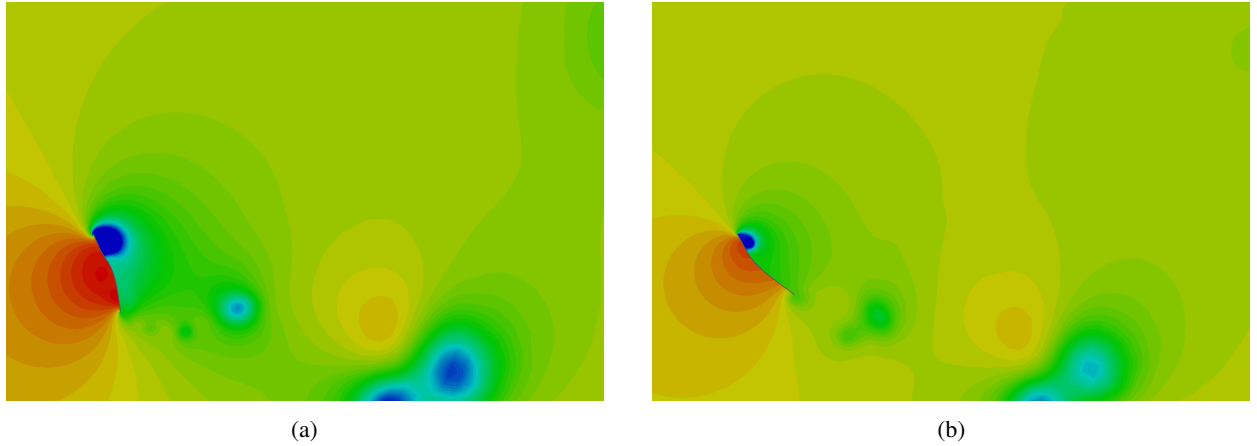

Figure 10: Pressure field at $t/T = 0.6$ with $f^* = 0.08$ and $\theta_0 = 90°$: (a) $\Sigma = 0.1$ and $\delta_p^* = 0.03$ and (b) $\Sigma = 10$ and $\delta_p^* = 0.0575$.

Using $f^* = 0.08$ and $\theta_0 = 90°$ as operating conditions, a large secondary peak of $C_{Y,\text{aero}}$ appears near $t/T = 0.4$ and $t/T = 0.9$ (Fig. 11a) which greatly contributes to the power extraction (see $C_{P,y}$ in Fig. 11b). This secondary peak is caused by a second LEV that only forms with flexible foils and that remains mostly a shear layer with the rigid

foil (Fig. 12). Because of the deformation, the Trailing-Edge Vortex (TEV) is directed upward and it has a stronger influence on the flow near the leading edge. The velocity induction of the TEV on the leading edge shear layer has the effect of generating the second LEV on flexible foils. Furthermore, the second LEV is pushed close to the foil's surface which results in a significant aerodynamic force increase.

In the case presented in Fig. 11, the pressure-induced deformation does not affect much $C_{M,\text{aero}}$ (Fig. 11a), however the horizontal aerodynamic force is greatly reduced which is beneficial not only on a mechanical design perspective, but also in the context where other turbines may be placed downstream. Indeed, reduced drag is generally associated with a more energetic wake behind a given turbine. Furthermore, the maximum vertical load is also reduced (at $t/T = 0.6$ on Fig. 11a). However, $C_{Y,\text{aero}}$ is largely increased near the top and bottom end of the cycle which, in overall, increases the mean power extraction coefficient while the overall aerodynamic force magnitude is reduced.
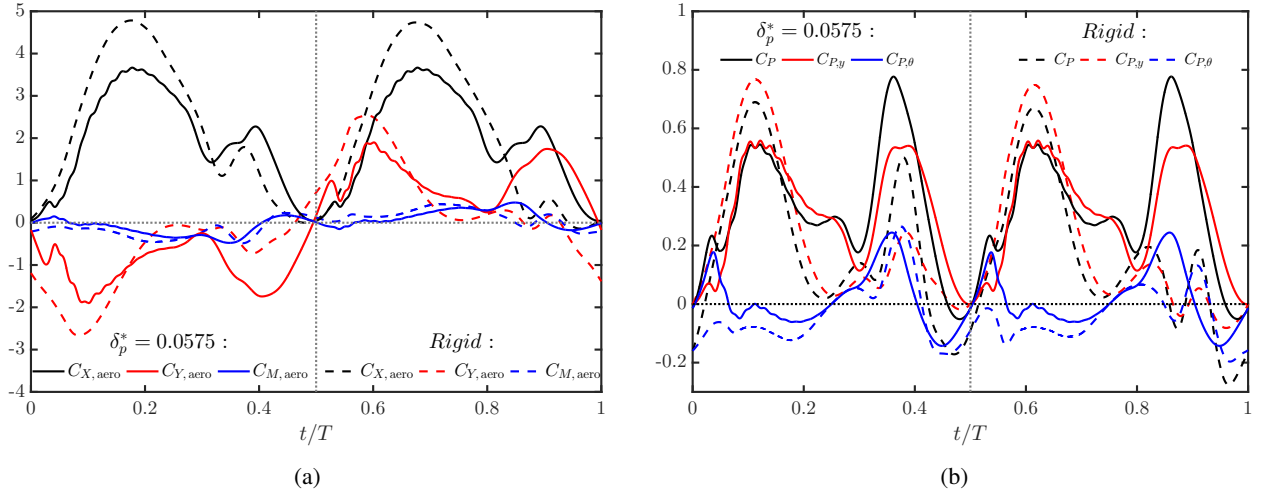
Figure 11: Instantaneous force and power coefficients for a typical pressure-driven deformation case with $\Sigma = 10$, $f^* = 0.08$, and $\theta_0 = 90°$: (a) force coefficients, (b) power coefficients.

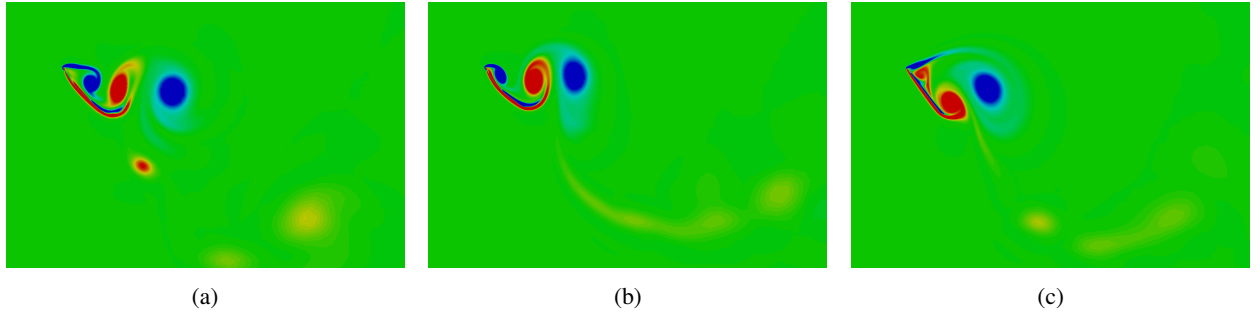Figure 12: Vorticity field at $t/T = 0.9$ with $f^* = 0.08$ and $\theta_0 = 90°$: (a) $\Sigma = 0.1$ and $\delta_p^* = 0.03$, (b) $\Sigma = 10$ and $\delta_p^* = 0.0575$, (c) rigid foil.

When there is no TEV (all cases simulated excepted when $f^* = 0.08$ and $\theta_0 = 90°$), the deformation caused by the LEV gets more and more important as the flexibility increases. This is depicted in Fig. 13 where the effects of the head and the tail deformations on the instantaneous angle of attack are shown by using the quantities $\Delta\alpha_{\text{head}}$ and $\Delta\alpha_{\text{tail}}$ (see Eq. (1)). The head is largely deformed when $t/T \approx 0.2$ and 0.7 (Fig. 13a), that is when the LEV forms. This large head deformation tends to increase α_{Eff} (in magnitude) and the LEV intensity. On the other hand, at the same time, the tail deformation reduces α_{Eff} (Fig. 13b) as it tends to align with the flow as a result of the feathering effect. When $t/T \approx 0.4$ and 0.9, the LEV reaches the trailing edge and pulls the tail up. The effective angle of attack is therefore largely decreased compared to the equivalent rigid foil (Fig. 14a) and even switches sign. The resulting vertical aerodynamic force is thus lower than that of a rigid foil (Fig. 14b) and it leads to a lower mean
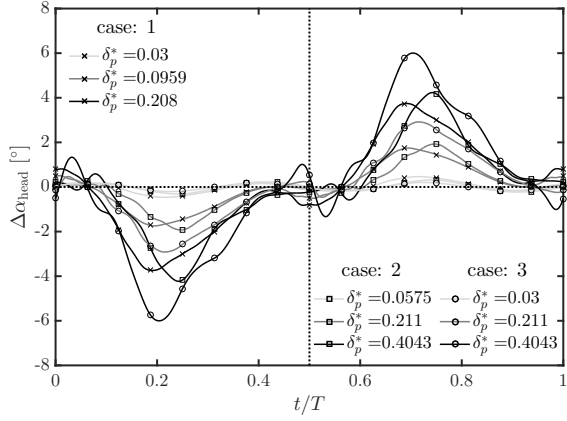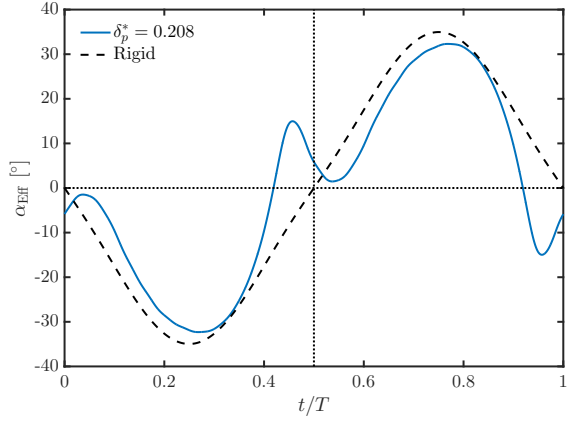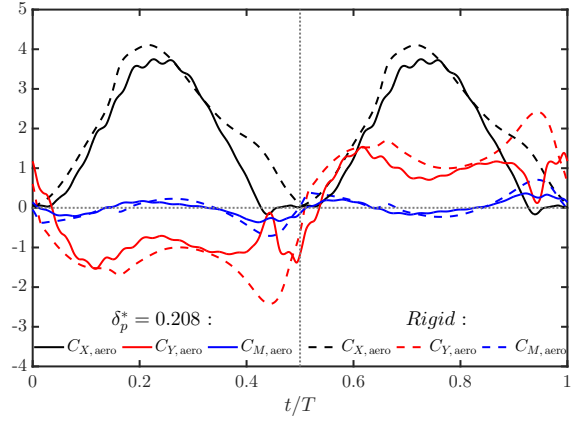
(a)
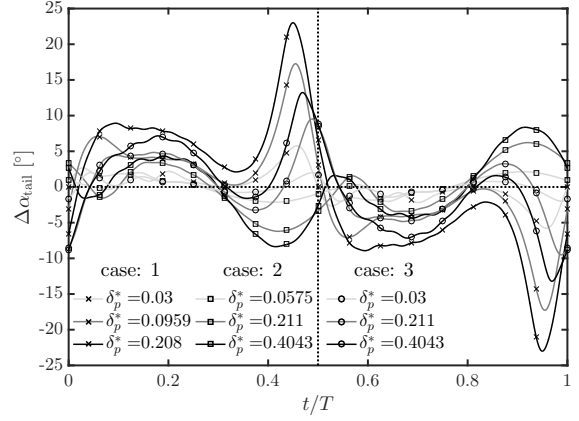
(b)

Figure 13: Effect of flexibility on the effective angle of attack: (a) head contribution, (b) tail contribution. Case 1: $f^* = 0.14$ and $\theta_0 = 76.3°$, Case 2: $f^* = 0.18$ and $\theta_0 = 60°$, and Case 3: $f^* = 0.14$ and $\theta_0 = 60°$.
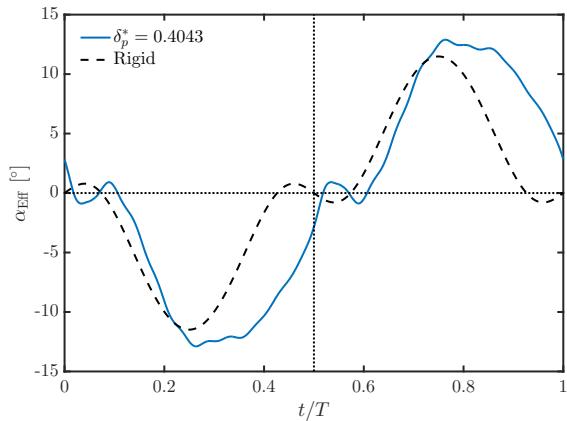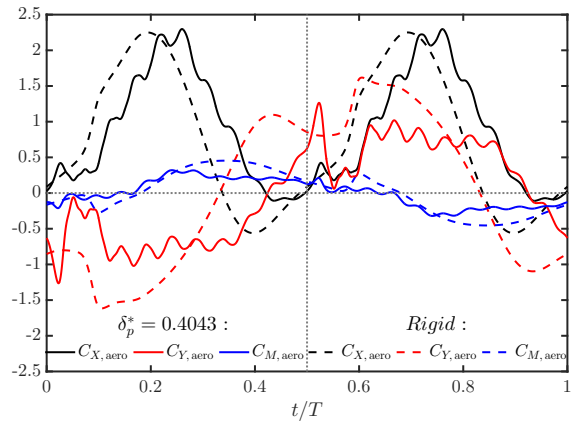

(a)

(b)

Figure 14: Comparison of a rigid foil and a flexible foil with $\Sigma = 10$ and $\delta_p^* = 0.208$: (a) effective angle of attack and (b) aerodynamic force coefficients. The motion parameters are $f^* = 0.14$ and $\theta_0 = 76.3°$.

(a)

(b)

Figure 15: Comparison of a rigid foil and a flexible foil with $\Sigma = 10$ and $\delta_p^* = 0.4043$: (a) effective angle of attack and (b) aerodynamic force coefficients. The motion parameters are $f^* = 0.18$ and $\theta_0 = 60°$.

15

power coefficient (Figs. 4a and 4d). However, Case 2 on Fig. 13 exhibits a different behavior of the tail near the top and bottom end of each cycle that benefits to the power extraction coefficient (reported on Fig. 4c for this case). The effective angle of attack keeps a higher value for a longer time compared to a rigid foil (Fig. 15a). It limits the periods where aerodynamic forces contribute negatively to the power extraction, i.e., when $C_{Y,\text{aero}}$ is positive in the first half cycle or negative in the second half cycle (Fig. 15b). As a result, the mean power coefficient is higher than that of a rigid foil (Fig. 4c).

4.1.3. Efficiency

As mentioned previously, the efficiency exhibits a different behavior than the mean power coefficient. For the configuration reported in Fig. 16, this is especially true when Σ is small. For example, when $\Sigma = 0.1$, the efficiency does not show any improvement compared to a rigid foil (Fig. 16) whereas the mean power coefficient is sometimes higher than that of a rigid wing with the same operating conditions (Fig. 4d). Recalling that the efficiency is proportional to $\overline{C_P}$ and $1/d$, the explanation is straightforward. The foil deformation increases more the vertical extent of the foil motion than the mean power coefficient which leads to a lower efficiency. This phenomenon is either less prominent or even completely mitigated when $\Sigma = 1$ and $\Sigma = 10$ because of the feathering effect which produces deformations that tend to reduce d. In fact, cases with $\Sigma = 10$ that exhibit a power increase generally present an efficiency increase as well.
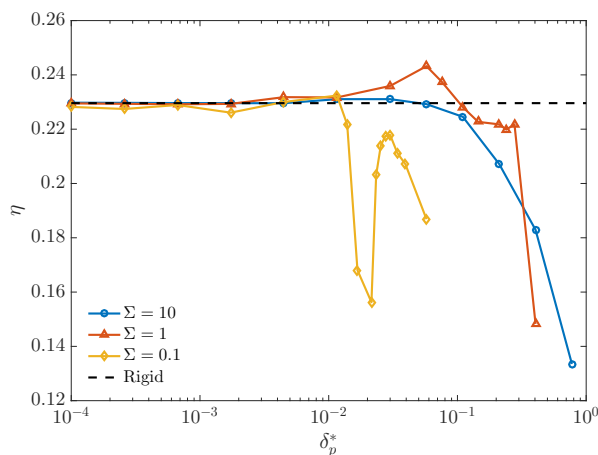

Figure 16: Efficiency for different δ_p^* and Σ for a completely flexible foil. In this example: $f^* = 0.14$ and $\theta_0 = 60°$.

4.2. Rear flexible foils

In this section, foils that have a flexible tail only are considered at two operating points. From the results presented in Fig. 17, it appears that pressure-driven deformations ($\Sigma = 10$) generally do not improve the mean power extraction coefficient and, when it does, the improvement remains rather small. On the other hand, Fig. 17b shows that $\overline{C_P}$ is improved by 20.2% when $\Sigma = 0.1$ and $\delta_p^* = 0.0347$ and by 18.3% when $\Sigma = 1$ and $\delta_p^* = 0.5089$. Thus, compared with a completely flexible foil (Fig. 4d), the rear flexible foil can reach larger improvements. Furthermore, rear flexible foils with $\Sigma = 1$ and $\Sigma = 0.1$ reach approximately the same optimal power coefficient (at different flexibilities though, see Fig. 17b) which is not the case for the completely flexible foil (see Fig. 4d). Indeed, the latter shows a lower optimal power coefficient when $\Sigma = 1$. Therefore, under these specific operating conditions ($f^* = 0.14$ and $\theta_0 = 60°$), the combination of front and rear flexibility is not optimal when $\Sigma = 1$. Also, it is worth pointing out that rear flexible foils have a power coefficient drop attributed to the excitation of the first mode of the tail that is similar to that of completely flexible foils when $\Sigma = 0.1$.

Inertia-driven deformations ($\Sigma = 0.1$) leads to some sort of a sinusoidal shaped α_{Eff} with a greater amplitude than that of a rigid foil whereas when $\Sigma = 1$, the effective angle of attack takes a relatively squared shape with a similar amplitude than that of a rigid foil (Fig. 18). When $\Sigma = 0.1$, the maximum vertical aerodynamic load is more than twice the one of a rigid foil. These aerodynamic forces (Fig. 19a) are very similar to those of a completely flexible foil
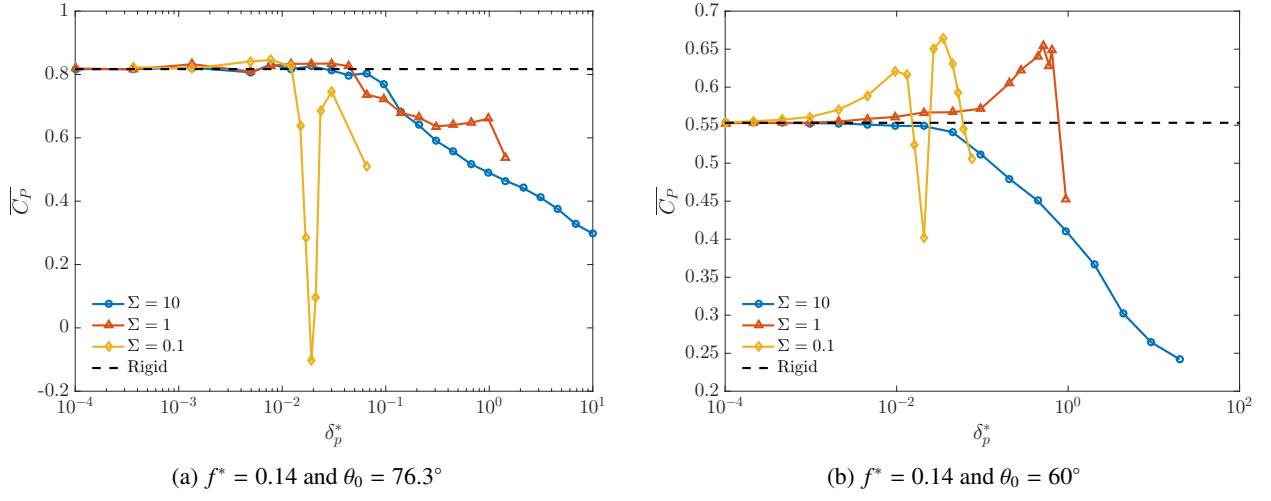
(a) $f^* = 0.14$ and $\theta_0 = 76.3°$ (b) $f^* = 0.14$ and $\theta_0 = 60°$

Figure 17: Mean power coefficient computed over the last cycle for different δ_p^* and Σ for a rear flexible foil.

(Fig. 8a) even if δ_p^* is slightly different, which means that the deformation of the tail is the main factor that improves the performances in the case of inertia-driven deformation. When $\Sigma = 1$ (Fig. 19b), the amplitudes of the aerodynamic loads are largely reduced compared to those at $\Sigma = 0.1$ (Fig. 19a). Nevertheless, the mean power extracted is almost the same. In this context, a design based on $\Sigma = 1$ would probably be a better option since it would produce weaker reactions on the driving mechanism (located at point P) which would be less demanding on a mechanical perspective.
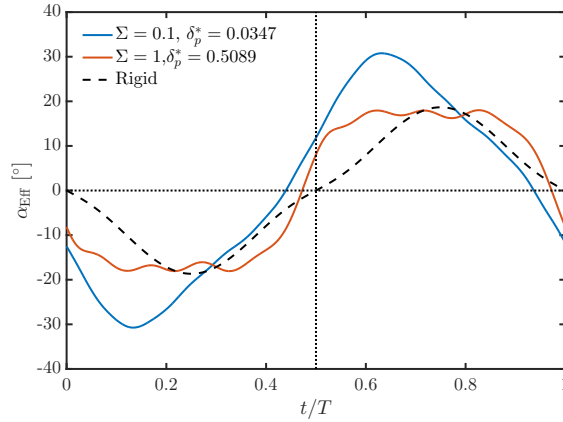

Figure 18: Effective angle of attack of the best cases at $\Sigma = 0.1$ and 1 compared with a rigid foil ($f^* = 0.14$, $\theta_0 = 60°$).

4.3. Front flexible foils

Front flexible foils power coefficients are reported in Fig. 20. These configurations also show a great potential with a maximum $\overline{C_P}$ improvement of 15% (Fig. 20b with $\Sigma = 1$ and $\delta_p^* = 0.2805$) compared to a rigid foil. Moreover, they exhibit the largest mean power coefficient of all cases tested in this study ($\Sigma = 0.1$ and $\delta_p^* = 0.0959$ in Fig. 20a). This maximum $\overline{C_P}$ appears to be a very sharp extremum on Fig. 20a. Similarly to what is reported in Section 4.1.1 for inertia-driven deformation cases, this highly localized variation of $\overline{C_P}$ against δ_p^* is caused by structural resonance. In this specific case, the first bending mode of the front flexible part of the foil is triggered by the fifth mode of the inertial force resulting from the driving motion. The larger amplitude and the better timing of $C_{Y,\,\text{aero}}$, that are direct consequences of both the LEV and the foil deformation, are the underlying reasons for this strong $\overline{C_P}$ with respect to δ_p^*. Therefore, the sensitivity of $\overline{C_P}$ on δ_p^* is very strong since punctual effects associated to resonance can significantly
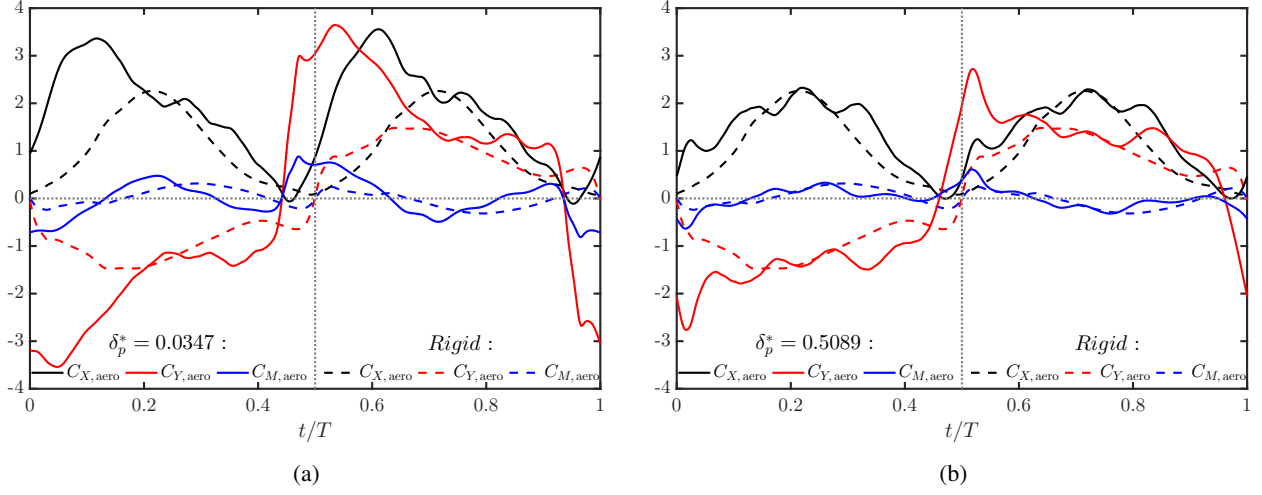
17

Figure 19: Aerodynamic force coefficients of the best cases of rear flexible foils with (a) $\Sigma = 0.1$ and (b) $\Sigma = 1$.
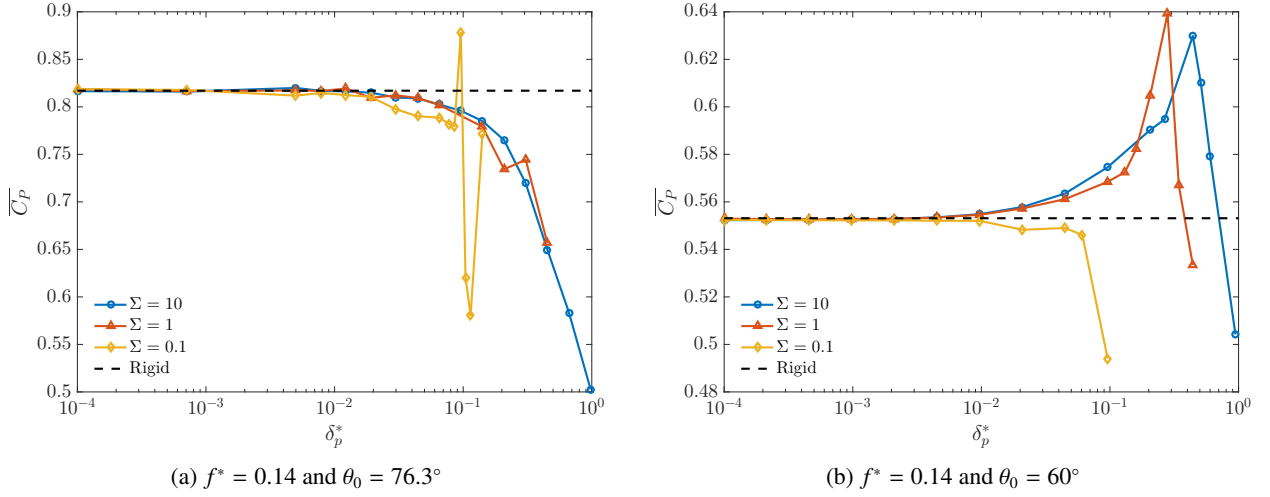

(a) $f^* = 0.14$ and $\theta_0 = 76.3°$

(b) $f^* = 0.14$ and $\theta_0 = 60°$

Figure 20: Mean power coefficient for different δ_p^* and Σ for a front flexible foil.

enhance or deteriorate the power extraction performance. Furthermore, comparing Fig. 4d with Fig. 20b it is found that front flexible foils performed better than completely flexible ones when $\Sigma = 1$. Therefore, this corroborates the previously mentioned fact that the combination of the head and tail flexibility is probably not optimal in this case.

Contrary to rear flexible foils, the effect of front flexibility on α_{Eff} is smaller which is mostly attributable to the fact that the pivot point is closer to the leading edge. Indeed, α_{Eff} keeps a relatively sinusoidal shape (Fig. 21), but with a different amplitude. The maximum effective angle of attack is usually shifted to the left compared to a rigid foil. As a result, the LEV of the front flexible foil is larger (Figs. 22a and 22b at $t/T = 0.75$). Nevertheless, the vertical aerodynamic force coefficient (Fig. 23) is not larger because the deformation orients the force along the x-axis which is confirmed by a larger $C_{X,\text{aero}}$. Around $t/T = 0.9$, $C_{Y,\text{aero}}$ of the front flexible foils exhibit a peak (Fig. 23). This peak is caused by the LEV that reaches the trailing edge (Fig. 22b at $t/T = 0.9$) and covers a large area whereas at the same time the LEV of the rigid foil has not reached the trailing edge yet.

Another interesting aspect of front flexibility is the fact that such configuration is unstable when Σ is high. Indeed, once a significant transverse pressure force occurs on the front part of the foil, the latter has the tendency to flip over and fold the foil such that it re-aligns itself with the flow. However, unless the foil is very flexible, it will not fold completely, which will results in potentially high pressure forces rather than a feathering effect. In fact, this
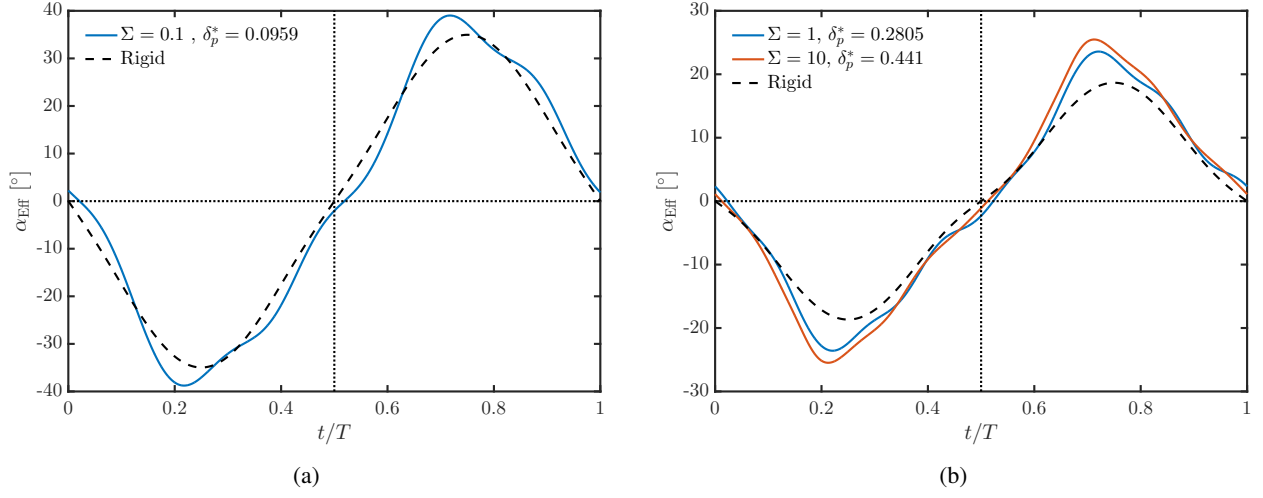
18

Figure 21: Effective angle of attack of the best cases of the front flexible foils: (a) $f^* = 0.14$ and $\theta_0 = 76.3°$ and (b) $f^* = 0.14$ and $\theta_0 = 60°$.

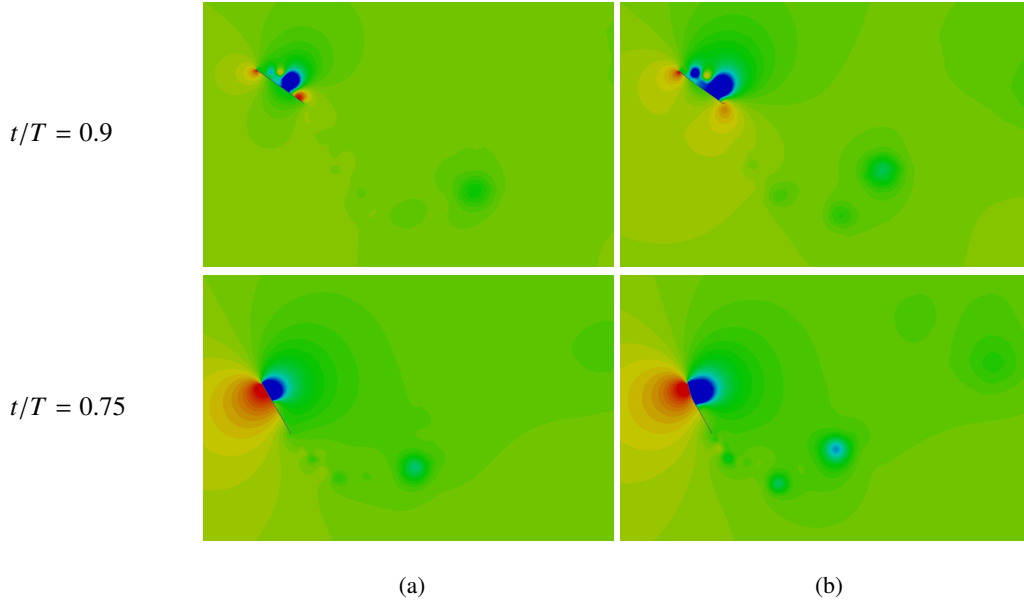Figure 22: Instantaneous pressure fields with $f^* = 0.14$ and $\theta_0 = 60°$ around (a) a rigid foil and (b) a front flexible foil ($\delta_p^* = 0.2805$ and $\Sigma = 1$).

(a) $\theta_0 = 76.3°$ and $\Sigma = 0.1$ (b) $\theta_0 = 60°$ and $\Sigma = 1$ (c) $\theta_0 = 60°$ and $\Sigma = 10$
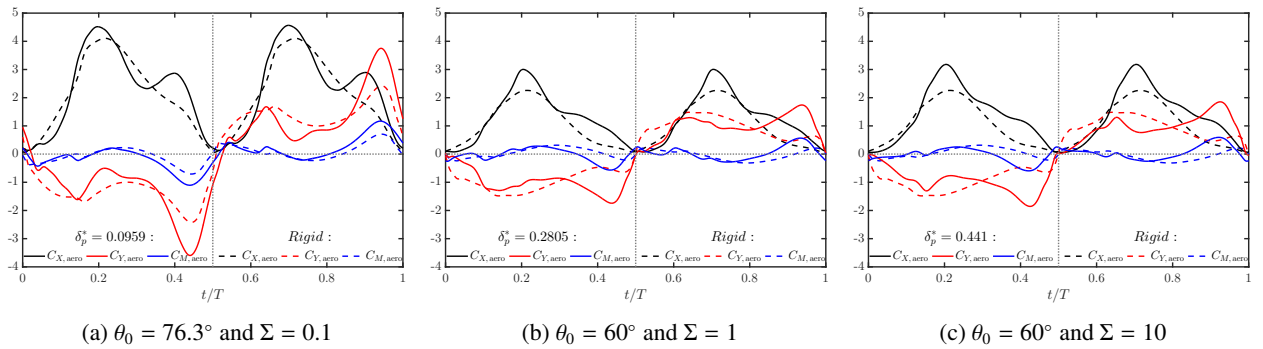
Figure 23: Aerodynamic force coefficients of some front flexible foils. $f^* = 0.14$ on all cases.

19

deformed configuration actually increases the effective angle of attack as depicted in Fig. 21b which results in higher aerodynamic forces (either $C_{X,\text{aero}}$ or $C_{Y,\text{aero}}$ depending on the force orientation, see Fig. 23c). Therefore, at moderate pitching angle, this reconfiguration mechanism can be used to increase passively the angle of attack and produce better power extraction as reported in Fig. 20b.

4.4. Comparison between rear and front flexible foils

As mentioned earlier, front or rear flexible foils can sometimes extract more power than a completely flexible foil ($\Sigma = 1$ in Figs. 4d, 17b, and 20b). This may be counter-intuitive as one could expect that if both front and rear flexibility taken independently increase the amount of power extracted, a completely flexible foil should show at least an equivalent performance. When comparing Figs. 17b and 20b, it appears that the maximum $\overline{C_P}$ at $\Sigma = 1$ is not reached at the same δ_p^* for front or rear flexible foils. Indeed, in this case, the rear flexible foil needs a higher flexibility ($\delta_p^* = 0.5089$) than a front flexible foil ($\delta_p^* = 0.2805$) to reach their respective maximum $\overline{C_P}$, which is quite comparable. Therefore, investigating foils with a higher flexibility on the rear part than on the front part could potentially lead to better energy extraction performances.

In addition, at relatively low pitching amplitude ($\theta_0 = 60°$), front and back flexible foils show an improvement in power extraction at different Σ values. Indeed, a large Σ benefits to front flexible foils (Fig. 20b) whereas a low Σ is profitable to rear flexible foils (Fig. 17b). In both cases, the flexibility helps in increasing the effective pitching angle, even though the deformation mechanisms are different. This improvement seems to vanish when the pitching angle is close to 76.3° as further increase in the effective pitching angle (hence, in the effective angle of attack) can hardly improve the power extraction from this point (except for the single configuration undergoing resonance in Fig. 20a). Lastly, Fig. 24 shows the evolution of the vertical aerodynamic force coefficient as well as the corresponding effective
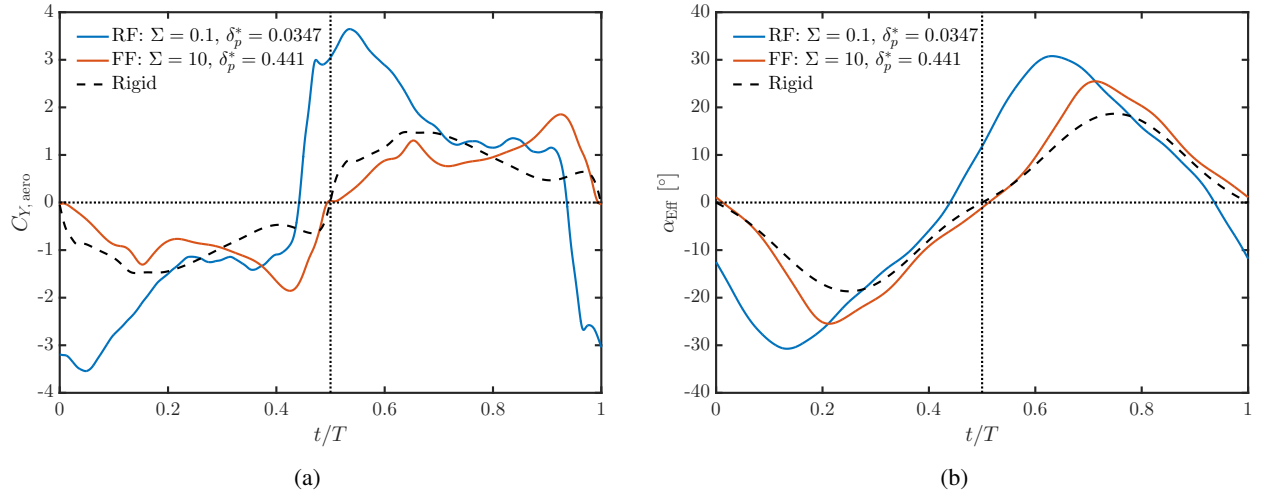

Figure 24: Comparison of (a) the vertical aerodynamic force coefficient and (b) the effective angle of attack for a rear flexible (RF) and front flexible (FF) foils with $f^* = 0.14$, $\theta_0 = 60°$.

angle of attack. It appears that inertia-based deformations of the rear part as well as pressure-based deformations of the front part can be used to tune the evolution of the effective angle of attack as these two mechanisms do not act at the same time during the cycle. Therefore, a foil with different mechanical properties (mass and rigidity) on the front and rear parts may eventually produced better performances than the cases presented in this study.

5. Conclusion

Numerical 2D numerical simulations of a chordwise flexible flapping-plate hydrokinetic turbine with a fully-coupled fluid-structure algorithm were performed. Results show that both pressure- and inertia-driven deformations on a front, rear, or completely flexible foil can improve the performances of such energy extraction devices. Indeed,

improvements of power coefficients of more than twice those of corresponding rigid foils have been recorded. Furthermore, the highest $\overline{C_P}$ within our parameter range is obtained with a front flexible foil that undergoes a resonance phenomenon.

Flexibility has the ability not only to modulate aerodynamic loads on the flapping foil, but also to shift the position of force extrema in time and, under some specific configurations, to create secondary force peaks. Low to moderate Σ configurations, i.e. mostly inertia-dominated deformations, generally result in an increase in aerodynamic forces magnitude. On the other hand, when Σ is large, the peaks of aerodynamic forces are usually reduced, but this reduction does not necessarily lead to lower performances in terms of power extraction. The general trends found in this research are that for rear and completely flexible foils, a low Σ is beneficial for relatively low pitching amplitude whereas high-Σ configurations perform better with high θ_0. On the other hand, front flexible foils perform better at high Σ when the pitching amplitude is low because of a reconfiguration mechanism.

Front or rear flexible foil may not reach their maximum $\overline{C_P}$ at the same δ_p^*. Therefore, considering that a completely flexible foil can benefit from both front and rear flexibility simultaneously, a larger δ_p^* for the rear than the front part of the completely flexible foil could possibly lead to enhanced performances compared to a uniform δ_p^*. In addition, the combination between Σ and the pitching amplitude also seems to play an important role. When considering a moderately small pitching amplitude (60° in this work), inertia-driven deformations are profitable to rear flexible foils whereas pressure-driven deformations benefit to front flexible wing. In both cases, the deformation results in an increased effective pitching angle. Increasing the amplitude to higher values mitigate the performance increase obtained with these two mechanisms.

The oscillation frequency appears to play an important role for flexible foils as it may excite bending modes. In the presented cases, the excitation of the first mode of the tail is produced by harmonics originating from the coupled pitching-and-heaving driving motion which appears to greatly deteriorate the power extraction potential in most cases. Indeed, even if high structural reactions on the driving point are produced at resonance, the amount of power extracted is low because the forces and the velocities are not in phase. On the other hand, resonance has been shown to produce an increase in power extraction on a specific front flexible case. Nevertheless, the effect of resonance being very sensitive to the natural frequency of the foil, hence to its flexibility, and to the driving frequency, it is not obvious that operating at a near resonance configuration is a practically viable solution.

Further investigation should focus on other operating conditions in order to have a better overview of the real potential of a flexible foil. Indeed, the parametric space of this problem is vast and this paper only covers a fraction of it. Moreover, simulations at higher Reynolds numbers would be interesting in order to characterize the effects of foil flexibility of a medium-to-large scale application. The effects of using a different non-uniform foil rigidity and density distributions should also be explored in a way that would combine the beneficial mechanisms observed in front and rear flexible foils investigated in this study.

Acknowledgments

References

Anderson, J., Streitlien, K., Barrett, D., Triantafyllou, M., 1998. Oscillating foils of high propulsive efficiency. Journal of Fluid Mechanics 360, 41–72.

Ashraf, M. a., Young, J., S. Lai, J. C., Platzer, M. F., jul 2011. Numerical Analysis of an Oscillating-Wing Wind and Hydropower Generator. AIAA Journal 49 (7), 1374–1386.
URL http://arc.aiaa.org/doi/abs/10.2514/1.J050577

Daniel, T., Combes, S., 2002. Flexible wings and fins: Bending by inertial or fluid-dynamic forces? Integrative and Comparative Biology 42, 1044–1049.

Dewey, P. A., Boschitsch, B. M., Moored, K. W., Stone, H. A., Smits, A. J., 10 2013. Scaling laws for the thrust production of flexible pitching panels. Journal of Fluid Mechanics 732, 29–46.
URL http://journals.cambridge.org/article_S0022112013003844

Epstein, M., Murray, D., 1976. Large deformation in-plane analysis of elastic beams. Computer and Structures 6, 1–9.

Heathcote, S., Gursul, I., Jan. 2005. Flexible flapping airfoil propulsion at low Reynolds numbers. In: 43th AIAA Aerospace Sciences Conference and Exhibit, paper AIAA-2005-1405. Reno, Nevada.

Heathcote, S., Gursul, I., 2007. Flexible flapping airfoil propulsion at low Reynolds numbers. AIAA Journal 45 (5), 1066–1079.

Hoke, C. M., Young, J., Lai, J. C. S., 2015. Effects of time-varying camber deformation on flapping foil propulsion and power extraction. Journal of Fluids and Structures 56, 152–176.

Kang, C., Aono, H., Cesnik, C., Shyy, W., 2011. Effects of flexibility on the aerodynamic performance of flapping wings. Journal of Fluid Mechanics 689, 32–74.

Katz, J., Weihs, D., 1978. Hydrodynamic propulsion by large amplitude oscillation of an airfoil with chordwise flexibility. Journal of Fluid Mechanics 88, 485–497.

Kinsey, T., Dumas, G., 2008. Parametric study of an oscillating airfoil in a power-extraction regime. AIAA Journal 46 (6), 1318–1330.

Kinsey, T., Dumas, G., 2012. Computational Fluid Dynamics Analysis of a Hydrokinetic Turbine Based on Oscillating Hydrofoils. Journal of Fluids Engineering 134 (2), 021104.

Kinsey, T., Dumas, G., 2014. Optimal operating parameters for an oscillating foil turbine at reynolds number 500, 000. AIAA Journal 52 (9), 1885–1895.

Kinsey, T., Dumas, G., Lalande, G., Ruel, J., Mehut, A., Viarouge, P., Lemay, J., Jean, Y., 2011. Prototype testing of a hydrokinetic turbine based on oscillating hydrofoils. Renewable energy 36 (6), 1710–1718.

Le, T. Q., Ko, J. H., 2015. Effect of hydrofoil flexibility on the power extraction of a flapping tidal generator via two- and three-dimensional flow simulations. Renewable Energy 80, 275–285.

Liu, W., Xiao, Q., Cheng, F., 2013. A bio-inspired study on tidal energy extraction with flexible flapping wings. Bioinspiration & biomimetics 8 (3), 036011.

Liu, W., Xiao, Q., Zhu, Q., 2016. Passive Flexibility Effect on Oscillating Foil Energy Harvester. AIAA Journal 54 (4), 1172–1187.
   URL http://arc.aiaa.org/doi/abs/10.2514/1.J054205

McKinney, W., DeLaurier, J., 1981. Wingmill: an oscillating-wing windmill. Journal of energy 5 (2), 109–115.

Olivier, M., 2014. A fluid-structure interaction partitioned algorithm applied to flexible flapping wing propulsion. Ph.D. thesis, Université Laval.
   URL http://www.theses.ulaval.ca/2014/30609/30609.pdf

Olivier, M., Dumas, G., 2016. A parametric investigation of the propulsion of 2d chordwise-flexible flapping wings at low reynolds number using numerical simulations. Journal of Fluids and Structures 63, 210 – 237.
   URL http://www.sciencedirect.com/science/article/pii/S0889974615300499

OpenFOAM Foundation, 2013. OpenFOAM - The Open Source CFD Toolbox - User Guide.
   URL http://www.openfoam.org/

Peng, Z., Zhu, Q., 2009. Energy harvesting through flow-induced oscillations of a foil. Physics of Fluids 21 (12), 1–9.
   URL http://dx.doi.org/10.1063/1.3275852http://scitation.aip.org/content/aip/journal/pof2/21/12?ver=pdfcov

Quinn, D. B., Lauder, G. V., Smits, A. J., 1 2014. Scaling the propulsive performance of heaving flexible panels. Journal of Fluid Mechanics 738, 250–267.
   URL http://journals.cambridge.org/article_S0022112013005971

Ramananarivo, S., Godoy-Diana, R., Thiria, B., 2011. Rather than resonance, flapping wing flyers may play on aerodynamics to improve performance. Proceedings of the National Academy of Sciences 108 (15), 5964–5969.
   URL http://www.pnas.org/content/108/15/5964.abstract

Shimizu, E., Isogai, K., Obayashi, S., 2008. Multiobjective Design Study of a Flapping Wing Power Generator. Journal of Fluids Engineering 130 (2), 021104.

Wu, J., Shu, C., Zhao, N., Tian, F. B., 2015a. Numerical study on the power extraction performance of a flapping foil with a flexible tail. Physics of Fluids 27 (1).

Wu, J., Wu, J., Tian, F.-B., Zhao, N., Li, Y.-D., 2015b. How a flexible tail improves the power extraction efficiency of a semi-activated flapping foil system: A numerical study. Journal of Fluids and Structures 54, 886–899.

Xiao, Q., Zhu, Q., 2014. A review on flow energy harvesters based on flapping foils. Journal of Fluids and Structures 46, 174–191.

Xu, M., Wei, M., Yang, T., Lee, Y. S., 2016. An embedded boundary approach for the simulation of a flexible flapping wing at different density ratio. European Journal of Mechanics, B/Fluids 55, 146–156.
   URL http://dx.doi.org/10.1016/j.euromechflu.2015.09.006

Young, D., Felgar, R., 1949. Tables of characteristic functions representing normal modes of vibration beam. The University of Texas Publication 44 (4913).

Young, J., Ashraf, M. a., Lai, J. C. S., Platzer, M. F., 2013. Numerical Simulation of Fully Passive Flapping Foil Power Generation. AIAA Journal 51 (11), 2727–2739.
   URL http://arc.aiaa.org/doi/abs/10.2514/1.J052542

Zhu, B., Han, W., Sun, X., Wang, Y., Cao, Y., Wu, G., Huang, D., Zheng, Z. C., 2015. Research on energy extraction characteristics of an adaptive deformation oscillating-wing. Journal of Renewable and Sustainable Energy 7 (2), 023101.

Zhu, Q., 2007. Numerical simulation of a flapping foil with chordwise or spanwise flexibility. AIAA Journal 45 (10), 2448–2457.

Zhu, Q., Peng, Z., 2009. Mode coupling and flow energy harvesting by a flapping foil. Physics of Fluids 21 (3).

Zhu, X., He, G., Zhang, X., 7 2014. How flexibility affects the wake symmetry properties of a self-propelled plunging foil. Journal of Fluid Mechanics 751, 164–183.
   URL http://journals.cambridge.org/article_S0022112014003103